Stability in turbulence: The interplay between shocks and vorticity in a superfluid with higher-order dispersion

M. E. Mossman [1], E. S. Delikatny [1], Michael McNeil Forbes [1,2,*] and P. Engels [1,†]

[1]*Department of Physics and Astronomy, Washington State University, Pullman, Washington 99164, USA*
[2]*Department of Physics, University of Washington, Seattle, Washington 98105, USA*

The dynamics of systems with higher-order dispersion are rapidly advancing to the center of modern hydrodynamics research. From natural shallow water waves and nonlinear optics to manufactured microcavity resonators, these systems offer many surprises that motivate both fundamental insights as well as new device paradigms. An extreme regime of hydrodynamics is the formation of shock waves where nonlinearities of the system further enhance the phenomenology. Higher-order dispersion can lead to novel dispersive shocks structures whose precise modeling is challenging current mathematical concepts. Here we present a seminal paper demonstrating, experimentally and numerically, the dynamics in an interacting superfluid with higher-order dispersion. Raman dressing, a technique which over recent years has emerged as a flexible tool to modify the dispersion, is used to induce spin-orbit coupling that features a region of negative effective mass. Intriguingly, the breaking of Galilean invariance by the spin-orbit coupling allows two different types of shock structures to emerge simultaneously in a single system. Furthermore, we describe an interplay between vortices and shock fronts leading to a surprising stability of one shock, which we attribute to reduced turbulence in regions of higher-order dispersion. Our paper suggests that spin-orbit coupling can be used as a powerful means to tune the effective viscosity in cold-atom experiments serving as quantum simulators of turbulent hydrodynamics with implications for quantum metrology, quantum information, photonic applications, and quantum simulations of neutron stars.

I. INTRODUCTION

Higher-order dispersions beyond the familiar parabolic form bring surprising and peculiar effects to hydrodynamic systems at the forefront of modern hydrodynamics research. These effects have many applications, including to shallow water waves, optical media, microcavity resonators, and photonic devices [1–6]. Nonlinearities can further enrich the phenomenology, leading to the formation of new shock structures that are only beginning to be explored [7]. Due to the complexity of the dynamics, these systems challenge existing mathematical models and pose many open questions for fundamental and applied studies.

Dilute-gas Bose-Einstein condensates (BECs) provide a powerful platform for studying these types of complex dynamics. By immersing a dilute-gas BEC into an appropriately tuned laser field, spin-orbit coupling (SOC) can be induced in the BEC [8–10]. This modifies the single-particle dispersion from a parabolic form $E(p) = p^2/2m$ to a double-well structure with higher-order terms, similar in form to band structures found in condensed-matter systems. Features of the dispersion can be tailored in experiments; by changing the intensity and relative detuning of the Raman beams, one can finely tune and manipulate the curvature of the dispersion.

A BEC with SOC constitutes an exotic medium through which topological defects, phonons, and shock waves can propagate. These features have characteristics that are strongly correlated with the properties of the underlying medium. For instance, in a conventional BEC, small-amplitude phonons propagate near the speed of sound in the medium at long wavelengths [11,12], and as the wavelength decreases, the propagation speed increases slightly [13]. However, in a BEC with SOC, the dispersion can be modified so that short-wavelength modes travel more slowly in specific directions. This has a profound impact on the shape of dispersive shock waves (DSWs) that develop from nonlinear interactions in the system. A prototypical example of this is demonstrated in Fig. 1 showing the results of a 1D numerical simulation using realistic SOC parameters which give rise to the dispersion shown in Fig. 2. Although a BEC with parabolic dispersion only supports shock structures akin to the left traveling one [14–16], qualitatively different structures, such as the right traveling one in Fig. 1, arise in the presence of a higher-order dispersion, which in this case lowers the phonon dispersion with positive momenta, slowing the speed of high-frequency components which now lag behind the shock front.

Directly imaging these features *in situ* in a realistic experiment is extremely challenging due to their submicron size. Here, we present alternative evidence, visible in current experiments, that robustly detects the asymmetry introduced by the SOC, looking at the macroscopic behavior of induced shock waves. The final narrative describes a subtle connection between the macroscopic hydrodynamic behavior and the microscopic dynamics of vortices.

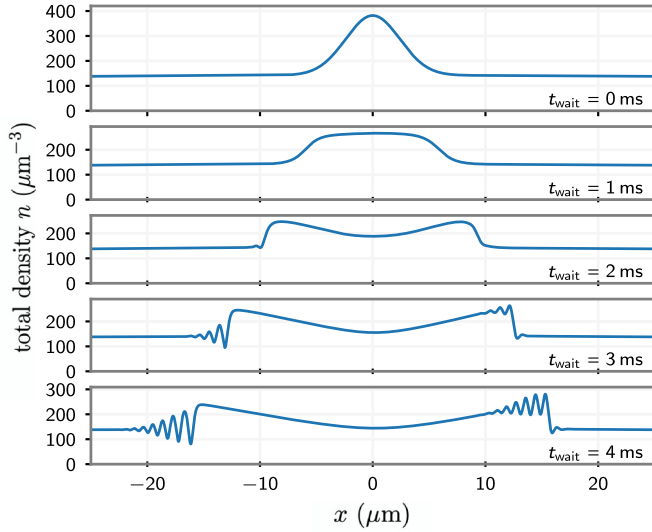---
*m.forbes@wsu.edu
†engels@wsu.edu

FIG. 1. The development of dispersive shock waves in a SOC BEC. At $t_{wait} \leqslant 0$ ms, this one-dimensional (1D) numerical simulation shows an initial density perturbation formed by an attractive Gaussian potential at the center of the system. The potential is suddenly switched off at $t_{wait} = 0$ ms and the initial density perturbation spreads outwards ($t_{wait} = 1$ ms), forming two traveling peaks ($t_{wait} = 2$ ms) and developing into DSWs moving in opposite directions ($t_{wait} = 3$ and 4 ms). The structure of a DSW is highly dependent on the background dispersion. In a SOC BEC, the breaking of Galilean invariance induces two distinct DSW structures in a single system: To the right, the solitary wave train lags behind the solitary wave edge (shock front), whereas to the left, the solitary wave train travels faster than the large amplitude shock front.
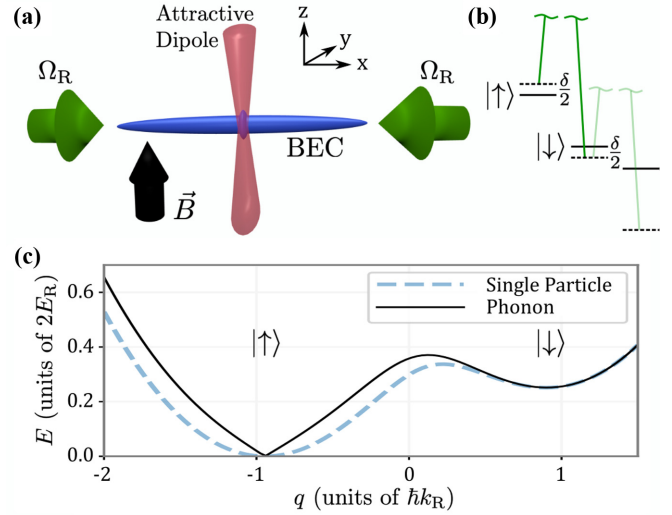

FIG. 2. Experimental setup. (a) An elongated BEC in a vertical magnetic field is prepared with spin-orbit coupling using two counter propagating Raman beams (green). An additional attractive optical potential (red) is applied at the center of the SOC BEC. (b) Raman beams couple the $|\uparrow\rangle$ and $|\downarrow\rangle$ pseudospin states in the $|F = 1\rangle$ manifold of ^{87}Rb. (c) The two-component excitation spectrum (black solid) and the single-particle dispersion (blue dashed) for our experimental parameters: $\Omega = 1.5E_R$ and $\delta = 0.54E_R$. The phonon dispersion has been shifted in the plot along the quasimomentum axis to line up with the single-particle dispersion minimum for convenience. The bulk speed of sound is $\approx \sqrt{gn/m}$ with small corrections from the SOC dispersion and mixing. To either side of the minima near $q = -1$, however, these corrections are small given the experimental parameters. The blue-shaded area indicates quasimomenta with negative effective mass.

Shock waves generated in a superfluid medium are typically considered to be dispersive (see Ref. [17] for a review): Instead of becoming infinitely steep, the shock front is smoothed by gradients in the kinetic energy (dispersion), and the energy in the shock wave is conserved. In direct contrast to this, classical shock waves are smoothed by dissipative effects, such as viscosity, which removes energy from the shock wave. Depending on the amplitude of the excitations and the geometry of the system, shock waves in a superfluid can decay into a variety of intricate structures determined by the dimensionality of the system [18], in part, due to the presence of snaking instabilities along transverse directions [19–22]. In one-dimensional systems, effectively realized in elongated trap geometries with tight radial confinement, superfluid shock waves remain dispersive [13,23,24]. As the dynamics probe additional dimensions, however, shock waves can appear to be dissipative, despite a lack of dissipation in the superfluid systems [25,26]. This effective viscosity arises from the generation of quantized superfluid vortices through snaking instabilities, resulting in a turbulent fluid that can be modelled by one-dimensional viscous shock wave (VSW) theory. We note that viscosity can appear in superfluids due to interactions with the normal component (mutual friction) and as intrinsic shear viscosity, but these effects are much smaller than those discussed here which can be reproduced with purely conservative simulations.

Here, we present a seminal study extending the realm of existing hydrodynamic experiments into the regime of excitation dynamics in the presence of higher-order dispersion. Our key results include: the description of a shock structure in a system with higher-order dispersion that presents many open questions for nonlinear science; the observation that—based on the breaking of Galilean symmetry—two different shock structures coexist in one and the same system; the surprising observation of a shock feature with solitonlike stability that forms in the region of higher-order dispersion; matching numerical simulations showing the source of this unlikely stability; and a study of excitation dynamics in the presence of quantum turbulence in a dilute-gas BECs, describing the intricate interplay between vortices and propagating shock structures. Our results reveal that SOC offers a flexible way to tune the effective viscosity of macroscopic hydrodynamics realized in turbulent quantum fluids, providing unmatched experimental control of turbulent hydrodynamics in cold-atom quantum simulators.

II. RESULTS

A. Experimental setup

To investigate the excitation dynamics, we employ an elongated BEC of ^{87}Rb atoms, confined in an optical dipole trap (see Appendix A for detailed experimental parameters). The

BEC is cigar shaped with an aspect ratio of approximately 100:1, and the long axis of the BEC is oriented horizontally as shown in Fig. 2(a). A uniform bias field in the z direction splits the $F = 1$ hyperfine ground state according to the Zeeman shift [Fig. 2(b)].

Spin-orbit coupling with its associated double-well dispersion, is induced by applying two counterpropagating Raman beams that couple the $|F, m_F\rangle = |1, -1\rangle$ and $|1, 0\rangle$ states, which we designate as two spin orientations $|\uparrow\rangle$ and $|\downarrow\rangle$ of a pseudospin-1/2 system, respectively [see Fig. 2(b) and Appendix A]. The height of the central hump in the single-particle dispersion (near quasimomentum $q = 0$ [see Fig. 2(c)]) depends on the Raman coupling strength Ω, which can be adjusted in the experiment by the intensity of the Raman beams I_R. The energetic offset of the two local minima of the dispersion depends on the detuning δ of the Raman coupling, which can be set by the frequency difference between the two Raman beams. The experimentally realized single-particle dispersion and the associated two-component phonon dispersion are shown in Fig. 2(c) by the dashed blue and solid black lines, respectively. See Appendix C for more information. Energies and momenta are measured in units of the recoil energy $E_R = \hbar^2 k_R^2 / 2m$ and recoil momentum $k_R = 2\pi/\lambda_R$, where λ_R is the Raman laser wavelength. The BEC is prepared with SOC such that the majority amplitude of atoms are in the $|\uparrow\rangle$ spin state and the direction of the SOC positive quasimomentum $+q$ is in the $+x$ direction as indicated in Fig. 2(a). Preparing the BEC with SOC causes heating in the system, reducing the the number of condensed atoms in the majority component to approximately 2×10^5 atoms. The atoms in the minority component $|\downarrow\rangle$ are indiscernible in the experimental images.

An additional dipole sheet aligned perpendicular to the long axis of the BEC creates an attractive Gaussian potential for the atoms at the center of the BEC. This vertical dipole sheet is pulsed on for 10 ms after the system has been prepared with SOC, resulting in excitations that propagate outwards along the along axis towards the edges of the BEC. The depth of this dipole potential U_b can be varied to generate large or small initial excitations in the BEC. In this section, U_b is on the order of the chemical potential of the majority component state ($|\uparrow\rangle$) in the SOC BEC $\mu = 95$ nK. To analyze the dynamics, absorption imaging is performed after a 10.1-ms time-of-flight (TOF) expansion. A Stern-Gerlach technique is used to vertically separate the spin states during the imaging procedure. Representative images obtained this way are presented in Fig. 3 where the $|\downarrow\rangle$ state is not shown due to low population of atoms in the minority component.

B. Experimental results

We have performed a systematic study of the dynamics following the sudden switch-off of the dipole sheet as a function of a subsequent in-trap evolution time t_{wait} and of the initial potential strength U_b. To better match the experimental results with numerics, we have introduced a wide cross-dipole beam to anchor the position of the SOC BEC in place during the experiment. This beam increases the axial trapping frequency to $2\pi \times 3.49$ Hz, leaving the radial trap frequencies unaltered but changing the aspect ratio of
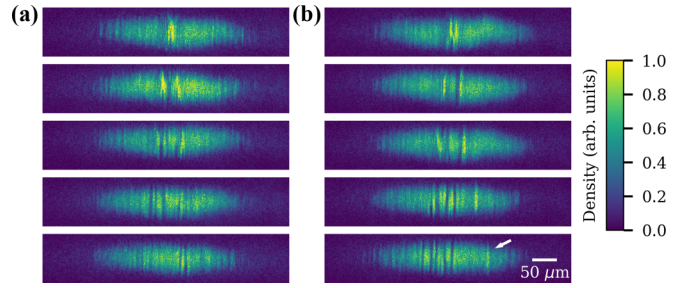

FIG. 3. Excitation dynamics with and without SOC. Absorption images acquired after a 10.1-ms time-of-flight expansion show the dynamics of outward moving excitations in a BEC prepared (a) without and (b) with SOC at times $t = 0$, 5 10, 25, and 40 ms (top to bottom) after a $U_b = -110$ nK $\approx -1.2\mu$ attractive potential has been applied to the center of the BEC for 10 ms. A Stern-Gerlach technique is used during time of flight to vertically separate the spin states in (b) where only the majority component is shown. The arrow in the last panel of (b) indicates a highly reproducible solitonlike peak propagating to the right, discussed in the main text.

the trap to approximately 80:1 and the chemical potential to $\mu = 55$ nK. A synopsis is presented in Fig. 4 and reveals the following features, the interpretation of which is confirmed by our matching numerical simulations: In the absence of SOC, the left-traveling and right-traveling excitations qualitatively behave in the same way as they propagate to the edges of the BEC, forming vortex rings and dark solitons. When strong SOC is applied to the system, parity is broken, and an asymmetric behavior is observed between the two directions. This asymmetric behavior is highly dependent on the depth of the initial potential with respect to μ and on the coupling strength of the SOC. For a system where the SOC coupling strength Ω and detuning δ are fixed, the following behavior is found:

(1) When $U_b < \mu$, excitations moving outwards from the center of the BEC display no discernible difference between the cases with and without SOC.

(2) When $U_b \gtrsim \mu$, the excitation propagating to the right consistently forms a well-defined peak that becomes particularly pronounced during the expansion dynamics and travels outward from the center towards the right edge of the cloud at a relatively constant velocity. For clarity, this peak is indicated with a white arrow in the lower right image of Fig. 3. Quantitative analysis of the right-traveling excitation yield experimental speeds of 1.63 ± 0.04 mm/s for $U_b = -30$ nK, 1.64 ± 0.05 mm/s for $U_b = -60$ nK, and 1.68 ± 0.06 mm/s for $U_b = -90$ nK. This excitation is highly reproducible and observed to have a lifetime comparable to small-amplitude excitations in past phonon excitation experiments [12,13,24]. In addition, solitonlike excitations are seen in the experimental images, and numerical simulations of the Gross-Pitaevskii equation (GPE) identify the generation of a collection of defects, including solitons, solitonic vortices, and vortex rings, during the 10-ms pulse of the attractive potential. The positions of these features depend subtly on small details, such as a tiny tilt in the dipole sheet or variations in the position of the potential, which are expected to vary in the experiment from shot to shot.
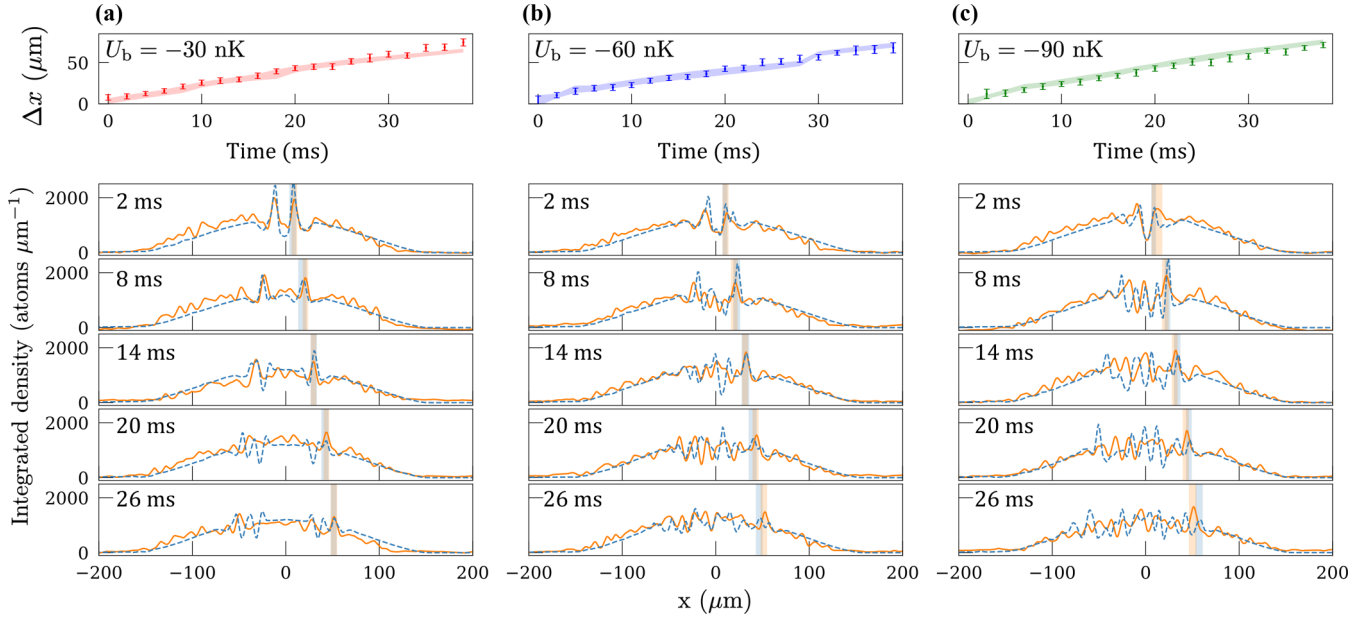
FIG. 4. Experimental results and numerical simulations. Analysis and integrated cross sections of an expanded BEC prepared in an elongated crossed-dipole trap with SOC after an attractive potential with (a) $U_b = -30$ nK, (b) $U_b = -60$ nK, or (c) $U_b = -90$ nK has been pulsed on at the center of the cloud for 10 ms. The chemical potential in the trap used here is $\mu = 55$ nK. After the potential is switched off, the system is allowed to evolve for a time t_{wait} in the presence of SOC prior to 10.1-ms time-of-flight expansion. The top row shows the position of the right moving excitation over time for GPE simulations (shaded region) and experiment (data points) for each potential depth, measured using a Gaussian fit function. The error bars and bands for both experiment and numerical results show the 2σ waist of the fitted Gaussian to the measured excitation. The experimental Gaussian waist presented here is comparable to the variation of the position of the shock feature shot to shot for similar experimental parameters. Quantitative results for the experiment are stated in the main text. In the lower panels, integrated cross sections for both GPE simulation (blue) and experiment (orange) are provided for each potential depth after $t_{wait} = 2, 8, 14, 20,$ and 26 ms where the shaded regions reflect the data presented in the top row. The GPE simulations presented here are performed using axial symmetry, which forces topological defects to align along the imaging axis. This results in some imaging defects from the numerical simulations, such as the slitting of the shock peak in the bottom two panels of the second column and corresponding kink in the top panel. For more information, see Appendix C. The simulations have been modified to reflect the optical resolution of the experiment (~ 2 μm) using a Gaussian convolution method.

C. Numerical results

To understand the experimental results, numerical simulations of a coupled set of GPEs are performed

$$i\hbar \frac{\partial}{\partial t} \begin{pmatrix} |\uparrow\rangle \\ |\downarrow\rangle \end{pmatrix} = \begin{pmatrix} \frac{\hat{p}^2}{2m} + V_\uparrow & \frac{\Omega}{2} e^{2ik_R x} \\ \frac{\Omega}{2} e^{-2ik_R x} & \frac{\hat{p}^2}{2m} + V_\downarrow \end{pmatrix} \cdot \begin{pmatrix} |\uparrow\rangle \\ |\downarrow\rangle \end{pmatrix}, \quad (1a)$$

$$V_{\uparrow/\downarrow} = -\left(\mu \pm \frac{\delta}{2}\right) + g_{\uparrow\uparrow/\uparrow\downarrow} n_\uparrow + g_{\uparrow\downarrow/\downarrow\downarrow} n_\downarrow, \quad (1b)$$

where $\hat{p} = -i\hbar\vec{\nabla}$ is the momentum operator, μ is the chemical potential in the SOC system, $g_{ab} = 4\pi\hbar^2 a_{ab}/m$, and a_{ab}'s are the s-wave scattering lengths (with $a, b = \uparrow$ or $\downarrow$). For ^{87}Rb, $a_{\uparrow\uparrow} = 100.40a_0$, $a_{\downarrow\downarrow} = 100.86a_0$, and $a_{\uparrow\downarrow} = 100.41a_0$ where a_0 is the Bohr radius. The system is prepared in the ground state with a Thomas-Fermi (TF) cloud radius of $x_{TF} = 150$ μm along the long axis, corresponding to $N_\uparrow = 206\,000$ and $N_\downarrow = 6000$ atoms in the condensate. The SOC parameters are $\Omega = 1.5E_R$ and $\delta = 0.54E_R$. To reduce computational costs, cylindrical symmetry is employed about the long axis of the trap. The system is evolved in real time following the experimental protocol including the imaging procedure, which we implement in an expanding coordinates system as discussed in Ref. [27]. See Appendix D for details.

This introduces some significant artifacts by restricting vortices to be vortex rings but allows us to fully simulate the experimental procedure including the expansion and imaging. Limited full three-dimensional (3D) simulations of the *in situ* dynamics confirming the behavior discussed here are shown in Fig. 5.

D. Interpretation of results

As demonstrated in the experimental absorption images of Fig. 3, a striking effect of the modified dispersion is the apparent stabilization of the right-moving shock wave, leading to a highly reproducible peak seen in the expansion images that is traveling to the right. The average Gaussian width of this shock feature is $w_s = 1.74 \pm 0.35$ μm when averaged over times $\{2, 4, 6, \dots, 46\}$ ms for all potential depths. This feature is reproduced by our numerical simulations, allowing us to probe the microscopic mechanism for this stabilization. Our numerics are summarized in Fig. 5. Details and animations can be found in Appendix E.

The numerics show the following progression of events. Shortly after turning on the attractive potential, fluid is drawn into the central region of the trap where the potential is located [Fig. 5(a)]. The subsequent flow induces a snaking instability
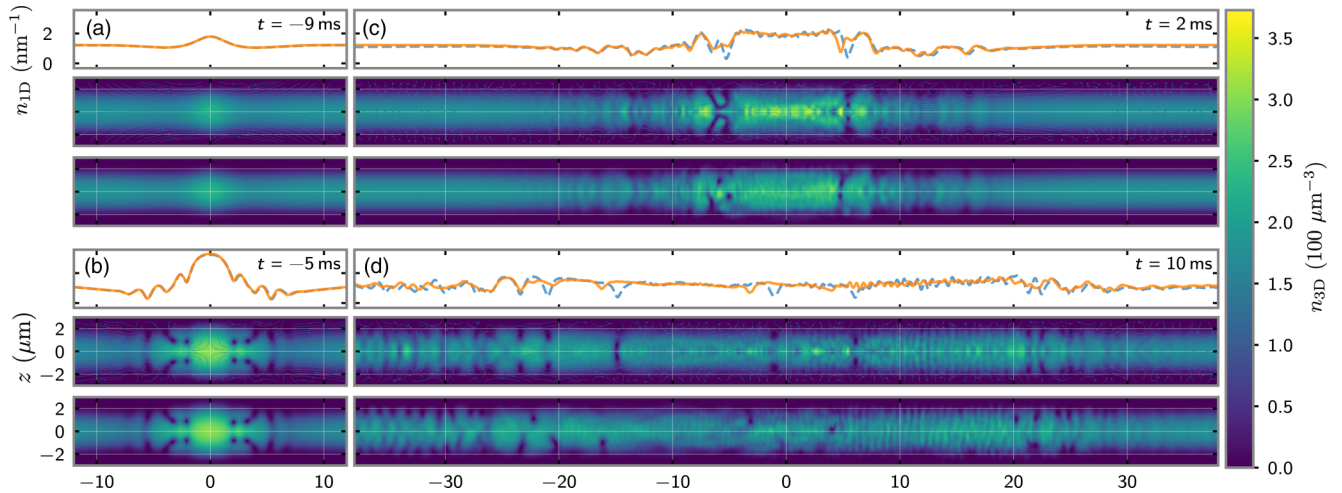
FIG. 5. Numerical simulations with and without spatial tilt of attractive potential. Simulated *in situ* images (prior to the expansion) of the four distinct stages of evolution from a simulation of the experiment with a -60-nK attractive potential. Here we compare axially symmetric simulations to 3D simulations with a small 1% y-tilted Gaussian dipole beam $V_{DB} \propto \exp{[(x + 0.01y)^2/2\sigma]}$. Upper frames are the integrated line-density $n_{1D}(x) = \int dy\,dz\,n(x, y, z)$ with axially symmetric data (blue), and 3D tilted data (orange). Middle frames are slices $n_{3D}(x, y) = n(x, y, 0)$ for axially symmetric simulations with streamlines of the current density $n_\uparrow \vec{v}_\uparrow + n_\downarrow \vec{v}_\downarrow$. Bottom frames are slices $n_{3D}(x, y) = n(x, y, 0)$ from the 3D tilted simulations. (a) Initial flow of the BEC into the region of the attractive potential. (b) Formation of several vortex rings due to snaking instabilities induced by this flow. The pattern of rings here is quite symmetric even in the tilted case. Vortex rings appear as reduced density in the 1D plots with mild dependence on the ring radius. (c) Formation of outgoing DSWs after the attractive potential is removed at $t = 10$ ms. In this frame, the DSWs are just starting to interacting with the first seeded vortex ring: Without the seeding rings, the structures of these DSWs are similar to that shown in Fig. 1. In the tilted case, the vortex rings rapidly decay into vortices that break the axial symmetry and average to significantly smoother integrated line density. (d) Results of DSWs interacting with initial vortex rings. Note that many fully formed and stable vortices exist on the left, whereas fewer vortices survive on the right. This is attributed to an increased number of vortex annihilation events to the right, evident by the manifestation of short wavelength oscillations in the integrated cross sections. Some features are sensitive to the tilt, such as the vortices near $x = 0$ whose location shifts by several microns in the integrated 1D density. Others remain robust, such as the right-moving shock wave and corresponding peak at 20–25 μm.

[19–22] seen in Fig. 5(b), forming vortex rings on either side of the growing central excitation, or bulge. During the initial stages of evolution, vortex rings form quite symmetrically on both sides. Most have their central flow oriented towards the center of the cloud, however, with increasing potential strength some vortex rings form with central flow facing outward.

After the attractive potential is turned off, the central bulge expands along the axis of the trap as shown in Fig. 5(c). This can be described by decomposing the bulge as a superposition of left- and right-moving bulges (phonons), which move outward at approximately the local speed of sound once the attractive potential is suddenly switched off. Due to the non-linear interaction, these left- and right-moving bulges quickly form DSWs, the orientation and polarization [17] of which are sensitive to the curvature of the dispersion as shown in Fig. 1. In particular, the left-moving DSW forms a leading soliton train as short-wavelength components travel faster than the solitary wave edge of the bulge. On the right, a small-wavelength soliton train trails behind the bulge. This has an intuitive explanation in terms of the modified dispersion. On the right, the phonon dispersion has negative curvature, and both group and phase velocities of the short-wavelength modes are *slower* [7,17]. Discerning these features in an experiment would require high-resolution *in situ* imaging as they are on the order of the healing length, and they do not survive the expansion imaging procedure.

As these outward traveling shock waves overtake the initially seeded vortex rings, intriguing dynamics ensue and a complex interaction develops between the rings and the shock front as shown in Fig. 5(d). In particular, the vortices absorb energy and momentum from the shock front, causing the shock to dissipate as if it were a VSW, even though the total energy is conserved by the system. To verify this, we have performed related simulations and experiments where the dipole beam is slowly turned on so as not to seed vortices: in this case, both shock waves persist, allowing us to conclude that the decay of the left-moving shock wave is, indeed, related to the presence of microscopic vorticity. This is consistent with previous observations of VSWs in superfluids as a result of dimensional reduction [25,26] where a dissipationless superfluid in 3D is described by viscous hydrodynamics in 1D after integrating over the transverse directions. The modified dispersion plays an important role here, significantly suppressing these dissipative effects. In Fig. 5(d) one can see a large number of vortex rings on the left side of the cloud, whereas very few remain on the right. Examining the detailed dynamics (see Appendix E), we see that vortex-vortex and vortex-shock front interactions are more likely to trigger vortex annihilation on the right side of the cloud than on the left. As a result, fewer vortices remain on the right, and less energy is dissipated from the shock front, leading to less effective viscosity and to the stabilization effect we observe in experiments with modified dispersion.

One might wonder if the asymmetry is due to the initial asymmetric form of the DSWs shown in Fig. 1, in particular, noting that the strong leading soliton train on the left might trigger the formation of more vortices. Although this likely plays a role, it appears that the vortices seeded in Fig. 5(b) are crucial to the observed dynamics, at least, at these potential strengths. Both numerics and experiment reveal that using a shallower potential, such as $U_b = -30$ nK [see Fig. 4(a)], decreases the number of defects generated initially in the system, thus, greatly reducing the effective viscosity, and shocks propagate in both directions without significant dissipation.

Explaining the exact microscopic mechanism for the enhanced likelihood of vortex annihilation with modified dispersion requires further investigation, but we anticipate that this is largely due to the presence of a dynamical instability in the region of negative effective mass [shaded region in Fig. 2(c)] [28]. As the shock front passes through a vortex ring, it can induce portions of its flow to enter this region where dynamical instabilities can manifest. Our numerics reveal that this often triggers the vortex ring to rapidly collapse or expand out of the system, effectively decaying to many high-frequency phonons seen as rapid near-stationery oscillations on top of the simulations in Fig. 5(d). In contrast, vortex interactions with the shock front moving to the left change the diameter of the vortex rings, triggering fewer annihilation events, and leaving them free to absorb the energy from the passing shock wave. Annihilations from the dynamical instability occur primarily in the center of vortex rings when the relative flow from the passing shock front increases the quasimomentum into the negative mass region. Notably, the rapid oscillations from the dynamical instability are also seen developing on the cusp of the outward traveling right side DSW in the raw $U_b = -30$-, -60-, and -90-nK numerical data sets.

E. Expansion dynamics

Structures induced by SOC and topological defects formed during DSW decay have length scales on the order of a healing length. These length scales are below the imaging resolution in our experimental setup. Therefore, time-of-flight imaging with 10.1-ms expansion time is used. During this expansion, features, such as solitons and vortices widen and, thus, can be resolved by the imaging system [29]. We have performed numerical simulations of the expansion dynamics which reveal that this process is nontrivial, and the structures of the excitations change considerably during this time. We find that the expansion process significantly enhances the peak of the DSWs, allowing it to be clearly imaged after the experiment: After the BEC is released from the trap, the gas expands rapidly in the radial direction, reducing the density by more than a factor of 10 in 2 ms and rendering the gas essentially noninteracting. In the remaining time of expansion, the various frequency components determined from the bare particle dispersion separate with velocity $v = \hbar k/m$, where k is the wave vector of the frequency component. What remains is a highly enhanced peak moving with the characteristic momentum of the shock wave. See Appendix F for more information and animations.

III. DISCUSSION

Using an attractive dipole sheet to generate large amplitude excitations on the background of a SOC BEC, we are able to probe the effects of higher-order dispersion on the nonlinear dynamics in an ultracold atomic system. The experimental results show a clear asymmetry in the nonlinear dynamics in the presence of SOC, surprisingly manifesting an enhanced stability of shock fronts propagating into the direction of higher-order dispersion, in agreement with GPE simulations. Within the numerical simulations, one is able to resolve the microscopic origin of this stability: The SOC significantly modifies the dynamics and stability of vortices in the region of modified dispersion, reducing their ability to dissipate energy from the shock wave. Although it has been shown that the presence of SOC significantly alters the structure of vortices [30], no comparable study of the effect on their dynamics has been performed.

The left-moving shock front decays rapidly, leaving behind a wake of vortices, whereas the right-moving shock front remains quite stable. We interpret the observed asymmetry as a manifestation of quantum turbulence: Viewed in terms of 1D VSW theory, the vorticity induced in the system provides a mechanism to absorb energy, resulting in an effective viscosity in the 1D theory, similar to that seen in previous superfluid experiments [25,26]. This effect is qualitatively consistent with our results, but further analysis is required to quantify the effective viscosity.

In this language, the modified dispersion here significantly alters the vortex dynamics in comparison to previous cited works, reducing the effective viscosity for the right-moving shock front. Thus, SOC provides an effective tool for modifying the underlying dynamics of vortices and thereby tuning the effective viscosity of the long-range hydrodynamic effective theory. Such control is essential for using cold atoms as effective quantum simulators for turbulent fluid dynamics with wide-ranging applications, including quantum metrology, quantum information, photonic applications, and quantum simulations of neutron stars. For example, quantum simulation using ultracold atoms is one of the most promising strategies for studying the hydrodynamics in neutron stars that result from quantum turbulence [31,32]. The neutrons, protons, and possibly even quarks in neutron stars form superfluids whose dynamics are thought to be responsible for observable phenomena, such as pulsar glitches—rapid sudden increases in the rotation rate of pulsars despite a stead loss of angular momentum. Being able to simulate neutron stars with terrestrial cold-atom experiments may provide the key needed to understand these glitches, whose microscopic origin remains a mystery, despite almost half a century of intensive study [33,34] (see Ref. [35] for a review). This application represents an exciting convergence of practical quantum simulation and improving astrophysical observations (see, for example, Ref. [36] where the structure of a glitch was observed).

Our results here show that spin-orbit coupling provides another tool to adjust the microscopic properties of quantum turbulence. Through proper calibration and benchmarking, such microscopic controls greatly expand the flexibility of

cold-atom platforms, allowing them to simulate other hydrodynamics systems with greater fidelity.

APPENDIX A: EXPERIMENTAL METHODS AND PARAMETERS

Our experiments are conducted with elongated BECs of ^{87}Rb atoms. The atoms are confined in an optical dipole trap with trap frequencies $\{\omega_x, \omega_y, \omega_z\} = 2\pi\{3.07, 278, 278\}$ Hz where the weakly confining direction is oriented horizontally. For data presented in Fig. 4, an additional wide cross-dipole beam anchors the BEC in place and increases the axial frequency from $2\pi \times 3.07$ to $2\pi \times 3.49$ Hz, whereas keeping the radial confinement the same. A 10-G uniform bias field leads to a Zeeman splitting of the hyperfine states. The $|1, -1\rangle$ and $|1, 0\rangle$ states are coupled through a two-photon Raman transition, whereas the $|1, +1\rangle$ state is essentially uncoupled due to the quadratic Zeeman effect. After loading into SOC, there are approximately 2×10^5 atoms in the majority ($|\uparrow\rangle$) component of the condensate. During the experiment, the Rabi coupling strength is $\Omega = 1.5 E_R$. The detuning of the Raman drive is set to $\delta = 0.54(1) E_R \equiv 2000(50)$ Hz where the uncertainty is given by the stability of the external bias field.

During the preparation and course of the experiment, heating caused by the Raman beams will decrease the condensate fraction, reducing the 1D longitudinal speed of sound and the equivalent non-SOC chemical potential in the majority component spin state from their initial values of $c_{s0} \approx 2.2$ mm/s and $\mu_0 \approx 100$ nK to $c_s \approx 1.6$ mm/s and $\mu \approx 55$ nK, respectively.

An additional vertical dipole sheet with $\lambda_b = 850$ nm and Gaussian waists $\{w_x, w_y\} = \{4.8, 27.2\}$ μm, is focused onto the center of the BEC. The extent of the Gaussian profile in the y direction is larger than the size of the BEC *in situ*. The beam is pulsed on for 10 ms to create excitations at the center of the cloud.

Imaging is performed after 10.1-ms time-of-flight expansion during which all laser beams are off, and a Stern-Gerlach technique is used to vertically separate the spin states during the imaging procedure.

APPENDIX B: GPE SIMULATIONS

To model the experiment, we adjust the chemical potential μ so that the density of the gas vanishes at $x_{TF} = 150$ μm in the TF approximation. These parameters correspond to a grid spacing of $dx \approx 0.06$ μm which is sufficiently small compared with the healing length $\xi \approx 0.22$ m in the center of the cloud.

We start from the ground state in a harmonic trap with frequencies $\{\omega_x, \omega_y, \omega_z\} = 2\pi\{3.49, 278, 278\}$ Hz. We then evolve in real time using a fifth-order Adams-Bashforth-Milne (ABM) predictor-corrector integration scheme [37] with stepsize $dt = 6.3$ μs. We model the dipole sheet with a Gaussian potential centered on x_0 with a width of $\sigma = 4.8$ μm. This potential is turned on and off smoothly using a C_∞ step function over $t_{step} = 0.1$ ms. We note that it is important for the accuracy of the ABM method that the time-dependent parameters vary smoothly.

To simulate the cloud expansion, we use the scaling procedure described in Ref. [27] to scale the radial coordinate without needing to add more lattice points to our simulation. Since the trapping potential along the long axis of the cloud is weak, there is very little expansion in this direction, so we do not scale the coordinate in this direction—our box is sufficiently large to accommodate this expansion.

Although the dynamics are three dimensional, the two radial trapping frequencies are approximately equal, and the full 3D dynamics are well approximated by an axially symmetric geometry. Axially symmetric simulations can reproduce turbulent features generated by a quantum-mechanical piston in a channel geometry, such as that found in Ref. [26]. Similar agreement between axially symmetric simulations [38] that can reproduce 3D shock phenomena in channel geometries [25] has also been observed in fermionic superfluids.

There are two differences of note between the experiment and GPE simulations. First, the numerical simulations enforce an axial symmetry, which restricts solitonic excitations, such as vortex rings, to be axially symmetric. Although this is consistent with the experimental geometry, it is well known that small perturbations will destabilize vortex rings, which can evolve relatively quickly into solitonic vortices [21,22,39–45]. We have verified by performing unrestricted 3D simulations (see Appendix F) that perturbations as small as 1% in alignment of the dipole beam (see the third panel of Fig. 5) rapidly induce these instabilities, resulting in much smoother average densities on the left consistent with the experimental images but performing full high-resolution simulations for direct comparison is prohibitive for this initial paper. We, therefore, expect that where the simulations produce vortex rings, we can expect to observe solitonic vortices in the experiment. Despite these radial instabilities, we have verified that using axially symmetric simulations still quantitatively reproduces the bulk dynamics in these elongated systems.

Second, whereas preparing the SOC BEC in the experiment, a thermal cloud is generated by the Raman beams in the initial state. This is observed in 1D cross sections of the data. Although in principle one can include the effects of the thermal cloud using the stochastic projected Gross-Pitaevskii equation (SPGPE) [46–49] or Zaremba-Nikuni-Griffin (ZNG) [50,51] formalisms, the agreement between our simulations and experiment show that these effects are small.

APPENDIX C: SOC PHONON DISPERSION

In a previous work, Khamehchi *et al.* used a single-particle dispersion to describe the expansion of a SOC BEC into a vacuum, notably matching the speed and DSW shape during expansion [28]. In contrast, here the DSW is expanding
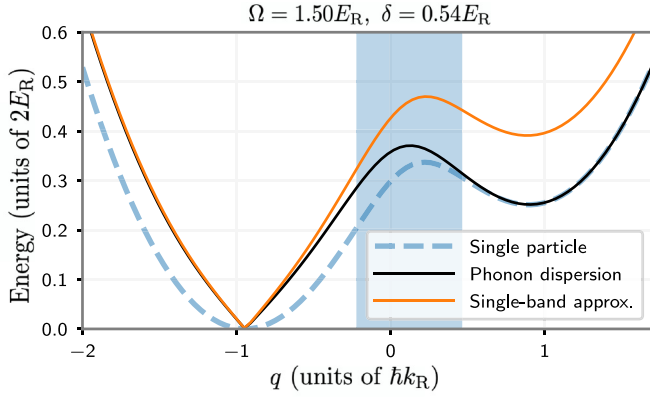
FIG. 6. Phonon dispersions with SOC. Phonon dispersion for the full theory (solid black curve) compared with the single-band approximation Eq. (C1) [solid orange (light gray) curve] and single-particle dispersion [thick blue (light gray) dashed curve] for experimental parameters $\Omega = 1.5E_R$ and $\delta = 0.54E_R$. The shaded area indicates quasimomenta with negative effective mass. The phonon dispersion has been shifted to line up with the single-particle dispersion minimum for convenience. Although qualitatively similar, the single-band model has some quantitative differences. For this reason, we simulate the full two-component model in all of our results.

through a nonzero background density. From this perspective, DSWs are large amplitude phonons described by a phonon dispersion constructed from Bogoliubov–de Gennes (BdG) theory.

The single-particle dispersion for excitations about the vacuum, used in Ref. [28], is found by solving

$$i = \sqrt{-1}\hbar \frac{\partial}{\partial t}|\psi\rangle = [E_{\pm}(\hat{p}) + gn + V_{\text{ext}}(x)]|\psi\rangle, \quad \text{(C1)}$$

where $E_{\pm}(\hat{p})$'s are the dispersion of the upper and lower bands of the single-particle obtained by diagonalizing Eq. (1) for homogeneous states. We assume that the coupling constants are equal $g_{\uparrow\uparrow} = g_{\downarrow\downarrow} = g_{\uparrow\downarrow} = g$. $|\psi\rangle$ is the wave function corresponding to the eigenstate of Eq. (1) describing the lowest band and is a linear combination of the two bare hyperfine states, and $n = n_{\downarrow} + n_{\uparrow}$ is the total density. For inhomogeneous densities this picture is locally valid for slowly varying densities, similar to the Thomas-Fermi approximation and remains valid as long as the system is gently excited compared to the band separation, which is proportional to the Raman coupling strength Ω. The two branches $E_{\pm}(p)$ mix the hyperfine states due to the SOC interaction,

$$\frac{\hbar E_{\pm}(\hbar k k_R)}{2E_R} = \frac{k^2 + 1}{2} \pm \sqrt{(k-d)^2 + w^2}, \quad \text{(C2)}$$

where we have defined the dimensionless parameters $k = p/\hbar k_R$, $d = \delta/4E_R$, and $w = \Omega/4E_R$ to incorporate Ω and the detuning of the Raman coupling δ. The form of the lower band defined here is shown as the dashed blue curve in Fig. 6.

With our given parameters, the single-band model exhibits qualitatively similar results to the multiband description where many aspects of the experiment are reproduced, but quantitative differences are observed. The approximate equality of the coupling constants allows one to define a spin-quasimomentum mapping that relates the two-component spin populations $n_{\uparrow}$ and $n_{\downarrow}$ to the quasimomentum q of the single-component state,

$$\frac{n_{\downarrow} - n_{\uparrow}}{n_{\downarrow} + n_{\uparrow}} = \frac{k - d}{\sqrt{(k-d)^2 + w^2}}. \quad \text{(C3)}$$

This simplified model captures the interesting phenomena observed in the experiment but is not quantitatively accurate.

Within this single-band model, the phonon dispersion obtained from BdG theory has a fairly simple form (thin solid orange curve in Fig. 6),

$$\omega(q) = E_1(q) + \sqrt{\frac{E_2(q)}{2}\left(\frac{E_2(q)}{2} + 2gn_0\right)}, \quad \text{(C4a)}$$

$$E_1(q) = \frac{E_-(q_0 + q) - E_-(q_0 - q)}{2}, \quad \text{(C4b)}$$

$$E_2(q) = E_-(q_0 + q) + E_-(q_0 - q) - 2E_-(q_0) \quad \text{(C4c)}$$

where n_0 is the background density upon which the phonons propagate, q_0 is the momentum of the background state, and q is the momentum of the phonon. Form these formulas the speed of sound follows from the slope of the dispersion at small momentum values. [For phonons about the ground state, one should take q_0 to be the minimum of the lowest band where $E'_-(q_0) = 0$ Eq. (C1).]

For our experimental parameters, this single-band theory predicts a linear dispersion for small phonon momenta and a rotonlike branch at large positive phonon momenta. These qualitative features persist in the two-component model, but to capture the full physics in the regions of negative mass, a two-component model is required. In particular, the phonon dispersion in the full two-component model shifts to a lower energy in the negative mass region, resulting in slower DSW propagation in the $+q$ direction, which gives rise to the asymmetry seen in Fig. 1.

The full phonon dispersion in the two-component model (black curve in Fig. 6) can be found by solving the following BdG equations,

$$\begin{pmatrix} K_{\uparrow}(q_0 + q) + g_{\uparrow\uparrow}n_{\uparrow} & g_{\uparrow\uparrow}n_{\uparrow} & \frac{\Omega}{2} + g_{\uparrow\downarrow}\sqrt{n_{\uparrow}n_{\downarrow}} & g_{\uparrow\downarrow}\sqrt{n_{\uparrow}n_{\downarrow}} \\ g_{\uparrow\uparrow}n_{\uparrow} & K_{\uparrow}(q_0 - q) + g_{\uparrow\uparrow}n_{\uparrow} & g_{\uparrow\downarrow}\sqrt{n_{\uparrow}n_{\downarrow}} & \frac{\Omega}{2} + g_{\uparrow\downarrow}\sqrt{n_{\uparrow}n_{\downarrow}} \\ \frac{\Omega}{2} + g_{\uparrow\downarrow}\sqrt{n_{\uparrow}n_{\downarrow}} & g_{\uparrow\downarrow}\sqrt{n_{\uparrow}n_{\downarrow}} & K_{\downarrow}(q_0 + q) + g_{\downarrow\downarrow}n_{\downarrow} & g_{\downarrow\downarrow}n_{\downarrow} \\ g_{\uparrow\downarrow}\sqrt{n_{\uparrow}n_{\downarrow}} & \frac{\Omega}{2} + g_{\uparrow\downarrow}\sqrt{n_{\uparrow}n_{\downarrow}} & g_{\downarrow\downarrow}n_{\downarrow} & K_{\downarrow}(q_0 - q) + g_{\downarrow\downarrow}n_{\downarrow} \end{pmatrix} \quad \text{(C5a)}$$

$$K_\uparrow(q) = \frac{(q + k_R)^2}{2m} - \mu - \frac{\delta}{2} + g_{\uparrow\uparrow} n_\uparrow + g_{\uparrow\downarrow} n_\downarrow,$$

$$K_\downarrow(q) = \frac{(q - k_R)^2}{2m} - \mu + \frac{\delta}{2} + g_{\uparrow\downarrow} n_\uparrow + g_{\downarrow\downarrow} n_\downarrow. \tag{C5b}$$

APPENDIX D: AXIALLY SYMMETRIC GPE SIMULATIONS

In Fig. 4 of the main text, experimental results are directly compared to a Gaussian convolution (to mimic the optical resolution of the experiment) of axially symmetric numerical GPE simulations. In this figure, the simulations show significant peaks moving to the left that are not observed in the experiments. This is due to the enforced axial symmetry in the simulations, forcing all defects to be aligned along the imaging axis. Symmetry unrestricted simulations (described in the following Appendix) show that small perturbations cause these defects to align quasirandomly, averaging out and only the shock fronts remain but are computationally expensive to perform for the full system, and although they are able to show an accurate picture of the experimentally observed dynamics, axially symmetric numerical simulations are able to reproduce some of the key macroscopic features observed in experiments. In this Appendix, we describe detail of these axially symmetric simulations with which we can simulate the full experiment, including expansion dynamics.

The simulations in Fig. 4 were performed using the axially symmetric GPE with a $N_x \times N_r = 8000 \times 50$ grid. The initial conditions use a cloud with a Thomas-Fermi radius of $x_{\text{TF}} = 150 \ \mu$m which models the condensate but not the extended thermal cloud. As has been noted in many experiments with BEC dynamics, we find again here that appropriately modeling the condensate without the thermal cloud provides an excellent approximation of the observed experimental dynamics. The three columns in Fig. 4 represent different potential depths -30, -60, and -90 nK, respectively.

Movies of these simulations are provided in the Supplemental Material [52] and include:

AXIAL30NK.MP4 [53]: Axially symmetric simulations without TOF expansion $U_b = -30$ nK.

AXIAL60NK.MP4 [54]: Axially symmetric simulations without TOF expansion $U_b = -60$ nK.

AXIAL90NK.MP4 [55]: Axially symmetric simulations without TOF expansion $U_b = -90$ nK.

SW.MP4 [56]: Shock waves from a 60-nK attractive potential interacting with vortex-antivortex line pairs of varying separation.

3D_90NK.MP4 [57]: A comparison between the Axial, "tube," 3D, and 3D 1%-tilt numerical simulations with an attractive potential depth of -90 nK.

AXIAL90NK_TOF.MP4 [58]: Axial simulation of 10.1-ms TOF expansion starting after 26 ms in trap evolution.

The simulated data in AXIAL30NK.MP4 [53], AXIAL60NK.MP4 [54], and AXIAL90NK.MP4 [55] show detailed dynamics of the system in three time regimes: First, from $t_{\text{wait}} = -10$ to 0 ms, showing the dynamic generation of turbulent features; second from $t_{\text{wait}} = 0$ to 6 ms, showing

the interaction between the DSW and the turbulent features stabilizing the right-hand side shock wave; third, from $t_{\text{wait}} = 6$ ms onward, showing the motion of the turbulent features once the density peak has passed.

The attractive potential is turned on at $t_{\text{wait}} = -10$ ms and the superfluid floods into the potential well, forming a large peak in the center. Within 2 ms, areas of modulated density form gray solitons at the edges of potential. For shallow potentials (-30 nK) these solitons are stable. However, for larger potential depths (-60 and -90 nK) a snaking instability sets in, nucleating vortex rings. The vortex rings form mostly with their central flow oriented away from the center of the cloud. This is clearly seen in the -30-nK simulation where all the vortex rings have a net outward flow and move in that direction. For larger potential heights, a few vortex rings of opposite orientation also form.

The vortex rings move according to the Magnus relation $\vec{v} \propto \vec{k} \times \vec{F}$, where $\vec{v}$ is the velocity of the vortex relative to the background flow, $\vec{k}$ is the circulation of the vortex, and $\vec{F}$ is a force acting on the vortex. If a vortex ring experiences a force in the same direction as its central flow, it will expand, whereas a vortex ring experiencing a force in the opposite direction to its central flow will shrink. In the present setting, the vortex rings see a background flow towards the attractive potential (altering $\vec{v}$) and a density gradient from the density peak ($\vec{F} = -\nabla gn$). The later density gradient moves outward as the shock features expand, causing vortex rings orientated away from density peak to expand, whereas shrinking vortex rings that are orientated towards it. For larger potential heights, nonequilibrium dynamics, including vortex ring collisions and annihilations, distort these features.

The attractive potential is turned off in 0.1 ms and at $t_{\text{wait}} = 0$ ms is completely off as the central density peak expands outward, pushing past the turbulent features. The density gradient widens (shrinks) vortex rings of same (opposite) central flow. If a ring becomes too small, it will annihilate through a Jones-Robert soliton [59–62]. Vortex rings with central flow oriented towards the SOC have a larger phase space to annihilate, leading to less vorticity, less effective viscosity, and less dissipation on the right-hand side. These vortex-shock interplay dynamics are explored in a systematic theoretical study captured in the video SW.MP4 [56]. Here, the vortex-antivortex separation and flow orientation are varied to represent a simplified view of the initial seeding of vorticity from jumping on the attractive potential. This simulation has been used to investigate the behavior of vortex line pairs as a shock structure passes through them with standard phonon dispersion (to the left) and higher-order phonon dispersion (to the right).

A closer look at the individual components around a vortex ring shows that areas with flow in the direction of the SOC

have higher densities of $|\downarrow\rangle$. As the density peaks pass through the vortex rings, the bump moving in the direction of the SOC converts particles from $|\uparrow\rangle$ to $|\downarrow\rangle$, whereas the bump traveling in the opposite direction converts particles from $|\downarrow\rangle$ to $|\uparrow\rangle$. For wait times longer than $t_{\text{wait}} = 8$ ms, the density bumps have developed DSW structures and the remaining vortex rings move according to the Magnus relation expected from their flow.

A deficiency of these axially symmetric simulations is that, in them, the vortex rings align perfectly with the imaging axis. This produces sharp features in the final images that would be averaged out by the line-of-sight imaging in experiments where perfect axial symmetry cannot be maintained. A clear example is seen in Fig. 4(b) in the $t_{\text{wait}} = 20$- and 26-ms frames. As can be seen from the movies, at these times, the large shock excitation moves through a vortex ring. The ring alters the integrated density, causing the shock image to split into two peaks separated by a density depletion from the vortex core. The peak-tracking algorithm finds the higher of these two peaks, which lags behind the center of the shock structure. Once the shock passes the ring, the right peak becomes larger, resulting in a kink in the top panel of Fig. 4(b) in the numerical (blue shaded) results. Without this artifact of the axial symmetry, we expect that the shock peak would follow the experimentally seen peak even more accurately.

APPENDIX E: AXIAL VS 3D NUMERICS

In addition to the full axial simulations described above, we have also performed 3D calculations. Full resolution 3D calculations are expensive, so for the unconstrained 3D analysis, we simulate only a central portion of the 3D BEC in a smaller box with $L_x = 120$ μm, $N_{xyz} = (1200, 64, 64)$, and a periodic trapping potential. This reduces the memory costs by a factor of 4 and is accurate for short times and dynamics in the center of the cloud as we ensure by comparing 3D simulation with symmetric initial condition to the full axial simulations described above. In some cases, a quasi-1D simulation using techniques, such as the nonpolynomial Schrödinger equation (NPSEQ) [44,63–65] and dynamically reduced GPE [66] (which we refer to as tube simulations) can quantitatively reproduce the 3D dynamics. However, these are insufficient once features, such as vortices appear as shown in Ref. [67].

Comparing 3D to axially symmetric simulations in 3D_90NK.MP4 [57], we see almost exact agreement during the 10-ms-long attractive potential pulse. This includes the formation of solitons, vortices pulled in from the boundary, and the snaking creation of vortex rings. The simulations differ as the density peak splits and pushes past the central vortices: The 3D simulations allow for more vortices to remain. However, there is agreement among the shape, speed of the shocks, the speed of solitonic, and vortex features.

To test the stability of vortex rings against small changes of the experimental parameters, we simulated the attractive dipole beam with a 1% tilt in the y direction, $V_{\text{DB}} \propto \exp\left[(x + 0.01y)^2/2\sigma\right]$. In this data (Fig. 5 third panel) and supplementary animations, we see that main features, such as the DSW maintain their structure. However, many of the vortex rings decay into vortex lines that terminate at the cloud edge. We find that the exact pattern of vortex generation depends very sensitively on the degree of this tilt, indicating that the underlying dynamics may be chaotic. This sensitivity is one hallmark of turbulent flow, supporting our interpretation of the observed macroscopic dynamics in terms of quantum turbulence.

APPENDIX F: TIME-OF-FLIGHT DYNAMICS

The technique used to numerically simulate the expansion of the system during the 10-ms time-of-flight corresponds to setting $\lambda_1(t) = 1$ and $\lambda_2(t) = \lambda_3(t) = \lambda_\perp(t)$ in Eqs. (11) and (15) of Ref. [27]. The evolution of dynamics during time of flight is shown in AXIAL90NK_TOF.MP4 [58].

When the Raman lasers inducing the SOC are switched off, the system is projected into the undressed basis of states $|\uparrow\rangle$ and $|\downarrow\rangle$. Without SOC to dress their momenta, the $|\uparrow\rangle$ component moves slowly to the right whereas the $|\downarrow\rangle$ component moves rapidly to the left, making it difficult to locate the center of the cloud. This can be understood in terms of the background ground state which is a linear combination of mostly $|\uparrow\rangle$ (with density $n_\uparrow$) having momentum $k_\uparrow = k_0 + k_R$ and some $|\downarrow\rangle$ (with density $n_\downarrow$) having momentum $k_\downarrow = k_0 - k_R$. The spin-quasimomentum map ensures that the background has zero net momentum: $n_\uparrow k_\uparrow + n_\downarrow k_\downarrow = (n_\uparrow + n_\downarrow)k_0 + (n_\uparrow - n_\downarrow)k_R = 0$. With our detuning, $n_\uparrow > n_\downarrow$ and $k_0 \approx -0.945 k_R$. Thus, during expansion, the two components move in opposite horizontal directions in addition to the vertical separation from the Stern-Gerlach technique. Within the first 2 ms of expansion the cloud expands rapidly, dropping the density by a factor of 10. The most notable features after expansion come from low-density objects, such as solitons, vortex rings, and DSW where areas with these features deepen and widen, pushing density to either side. The density pileup of nearby vortex rings will often constructively interfere, resulting in some of the largest peaks during expansion dynamics.

[1] A. Mohamadou, C. G. LatchioTiofack, and T. C. Kofané, Wave train generation of solitons in systems with higher-order nonlinearities, Phys. Rev. E **82**, 016601 (2010).

[2] S. Malaguti, M. Conforti, and S. Trillo, Dispersive radiation induced by shock waves in passive resonators, Opt. Lett. **39**, 5626 (2014).

[3] G. A. El and N. F. Smyth, Radiating dispersive shock waves in non-local optical media, Proc. R. Soc. A **472**, 20150633 (2016).

[4] M. Liu, L. Wang, Q. Sun, S. Li, Z. Ge, Z. Lu, C. Zeng, G. Wang, W. Zhang, X. Hu, and W. Zhao, Influences of high-order dispersion on temporal and spectral properties of microcavity solitons, Opt. Express **26**, 16477 (2018).

[5] Y. Zhao, X. Ji, B. Y. Kim, P. S. Donvalkar, J. K. Jang, C. Joshi, M. Yu, C. Joshi, R. R. Domeneguetti, F. A. S. Barbosa, P. Nussenzveig, Y. Okawachi, M. Lipson, and A. L. Gaeta, Visible nonlinear photonics via high-order-mode dispersion engineering, Optica **7**, 135 (2020).

[6] A. F. Fercher, W. Drexler, C. K. Hitzenberger, and T. Lasser, Optical coherence tomography - principles and applications, Rep. Prog. Phys. **66**, 239 (2003).

[7] P. Sprenger and M. A. Hoefer, Shock waves in dispersive hydrodynamics with nonconvex dispersion, SIAM J. Appl. Math. **77**, 26 (2017).

[8] Y.-J. Lin, R. L. Compton, A. R. Perry, W. D. Phillips, J. V. Porto, and I. B. Spielman, Bose-Einstein Condensate in a Uniform Light-Induced Vector Potential, Phys. Rev. Lett. **102**, 130401 (2009).

[9] Y. J. Lin, K. Jimenez-Garcia, and I. B. Spielman, Spin-orbit-coupled Bose-Einstein condensates, Nature (London) **471**, 83 (2011).

[10] Y. Zhang, M. E. Mossman, Th. Busch, P. Engels, and C. Zhang, Properties of spin–orbit-coupled Bose-Einstein condensates, Front. Phys. **11**, 118103 (2016).

[11] N. N. Bogolyubov, On the theory of superfluidity, J. Phys. (USSR) **11**, 23 (1947).

[12] M. R. Andrews, D. M. Kurn, H.-J. Miesner, D. S. Durfee, C. G. Townsend, S. Inouye, and W. Ketterle, Propagation of Sound in a Bose-Einstein Condensate, Phys. Rev. Lett. **79**, 553 (1997).

[13] J. J. Chang, P. Engels, and M. A. Hoefer, Formation of Dispersive Shock Waves by Merging and Splitting Bose-Einstein Condensates, Phys. Rev. Lett. **101**, 170404 (2008).

[14] B. Damski, Formation of shock waves in a Bose-Einstein condensate, Phys. Rev. A **69**, 043610 (2004).

[15] B. Damski, Shock waves in a one-dimensional bose gas: From a Bose-Einstein condensate to a Tonks gas, Phys. Rev. A **73**, 043601 (2006).

[16] M. A. Hoefer, M. J. Ablowitz, I. Coddington, E. A. Cornell, P. Engels, and V. Schweikhard, Dispersive and classical shock waves in Bose-Einstein condensates and gas dynamics, Phys. Rev. A **74**, 023623 (2006).

[17] G. A. El and M. A. Hoefer, Dispersive shock waves and modulation theory, Physica D **333**, 11 (2016).

[18] P. G. Kevrekidis, D. J. Frantzeskakis, and R. Carretero-González, *The Defocusing Nonlinear Schrodinger Equation: From Dark Solitons to Vortices and Vortex Rings*, Other Titles in Applied Mathematics (Society for Industrial and Applied Mathematics, Philadelphia, 2015).

[19] E. Kuznetsov, A. Rubenchik, and V. Zakharov, Soliton stability in plasmas and hydrodynamics, Phys. Rep. **142**, 103 (1986).

[20] A. Muryshev, G. V. Shlyapnikov, W. Ertmer, K. Sengstock, and M. Lewenstein, Dynamics of Dark Solitons in Elongated Bose-Einstein Condensates, Phys. Rev. Lett. **89**, 110401 (2002).

[21] J. Brand and W. P. Reinhardt, Solitonic vortices and the fundamental modes of the "snake instability": Possibility of observation in the gaseous Bose-Einstein condensate, Phys. Rev. A **65**, 043612 (2002).

[22] M. A. Hoefer and B. Ilan, Onset of transverse instabilities of confined dark solitons, Phys. Rev. A **94**, 013609 (2016)PRAHC3.

[23] M. A. Hoefer, P. Engels, and J. J. Chang, Matter-wave interference in bose-einstein condensates: A dispersive hydrodynamic perspective, Physica D **238**, 1311 (2008).

[24] R. Meppelink, S. B. Koller, J. M. Vogels, P. van der Straten, E. D. van Ooijen, N. R. Heckenberg, H. Rubinsztein-Dunlop, S. A. Haine, and M. J. Davis, Observation of shock waves in a large Bose-Einstein condensate, Phys. Rev. A **80**, 043606 (2009).

[25] J. A. Joseph, J. E. Thomas, M. Kulkarni, and A. G. Abanov, Observation of Shock Waves in a Strongly Interacting Fermi Gas, Phys. Rev. Lett. **106**, 150401 (2011).

[26] M. E. Mossman, M. A. Hoefer, K. Julien, P. G. Kevrekidis, and P. Engels, Dissipative shock waves generated by a quantum mechanical piston, Nat. Commun. **9**, 4665 (2018).

[27] Y. Castin and R. Dum, Bose-Einstein Condensates in Time Dependent Traps, Phys. Rev. Lett. **77**, 5315 (1996).

[28] M. A. Khamehchi, K. Hossain, M. E. Mossman, Y. Zhang, Th. Busch, M. M. Forbes, and P. Engels, Negative Mass Hydrodynamics in a Spin-Orbit–Coupled Bose-Einstein Condensate, Phys. Rev. Lett. **118**, 155301 (2017).

[29] B. P. Anderson, P. C. Haljan, C. A. Regal, D. L. Feder, L. A. Collins, C. W. Clark, and E. A. Cornell, Watching Dark Solitons Decay into Vortex Rings in a Bose-Einstein Condensate, Phys. Rev. Lett. **86**, 2926 (2001).

[30] J. Radić, T. A. Sedrakyan, I. B. Spielman, and V. Galitski, Vortices in spin-orbit-coupled Bose-Einstein condensates, Phys. Rev. A **84**, 063604 (2011).

[31] G. Greenstein, Superfluid turbulence in neutron stars, Nature (London) **227**, 791 (1970).

[32] A. Bulgac, M. M. Forbes, and G. Wlazłowski, Towards quantum turbulence in cold atomic fermionic superfluids, J. Phys. B: At. Mol. Phys. **50**, 014001 (2016).

[33] R. E. Packard, Pulsar Speedups Related to Cetastability of the Superfluid Neutron-Star Core, Phys. Rev. Lett. **28**, 1080 (1972).

[34] P. W. Anderson and N. Itoh, Pulsar glitches and restlessness as a hard superfluidity phenomenon, Nature (London) **256**, 25 (1975).

[35] B. Haskell and A. Melatos, Models of pulsar glitches, Int. J. Mod. Phys. D **24**, 1530008 (2015).

[36] G. Ashton, P. D. Lasky, V. Graber, and J. Palfreyman, Rotational evolution of the Vela pulsar during the 2016 glitch, Nat. Astronomy **3**, 1143 (2019).

[37] R. W. Hamming, *Numerical Methods for Scientists and Engineers* (McGraw-Hill, Inc., New York, 1973).

[38] F. Ancilotto, L. Salasnich, and F. Toigo, Shock waves in strongly interacting Fermi gas from time-dependent density functional calculations, Phys. Rev. A **85**, 063612 (2012).

[39] C. Becker, K. Sengstock, P. Schmelcher, P. G. Kevrekidis, and R. Carretero-Gonzalez, Inelastic Collisions of Solitary Waves in Anisotropic Bose-Einstein Condensates: Sling-Shot Events and Expanding Collision Bubbles, New J. Phys. **15**, 113028 (2013).

[40] M. D. Reichl and E. J. Mueller, Vortex Ring Dynamics in Trapped Bose-Einstein Condensates, Phys. Rev. A **88**, 053626 (2013).

[41] M. J. H. Ku, W. Ji, B. Mukherjee, E. Guardado-Sanchez, L. W. Cheuk, T. Yefsah, and M. W. Zwierlein, Motion of a Solitonic Vortex in the BEC-BCS Crossover, Phys. Rev. Lett. **113**, 065301 (2014).

[42] G. Wlazłowski, A. Bulgac, M. M. Forbes, and K. J. Roche, Life cycle of superfluid vortices and quantum turbulence in the unitary Fermi gas, Phys. Rev. A **91**, 031602(R) (2015).

[43] P. Scherpelz, K. Padavić, A. Rançon, A. Glatz, I. S. Aranson, and K. Levin, Phase Imprinting in Equilibrating Fermi Gases: The Transience of Vortex Rings and Other Defects, Phys. Rev. Lett. **113**, 125301 (2014).

[44] A. Muñoz Mateo and J. Brand, Chladni Solitons and the Onset of the Snaking Instability for Dark Solitons in Confined Superfluids, Phys. Rev. Lett. **113**, 255302 (2014).

[45] M. J. H. Ku, B. Mukherjee, T. Yefsah, and M. W. Zwierlein, Cascade of Solitonic Excitations in a Superfluid Fermi Gas: From Planar Solitons to Vortex Rings and Lines, Phys. Rev. Lett. **116**, 045304 (2016).

[46] C. W. Gardiner, J. R. Anglin, and T. I. A. Fudge, The stochastic Gross-Pitaevskii equation, J. Phys. B **35**, 1555 (2002).

[47] C. W. Gardiner and M. J. Davis, The stochastic Gross–Pitaevskii equation: II, J. Phys. B **36**, 4731 (2003).

[48] S. J. Rooney, P. B. Blakie, and A. S. Bradley, Stochastic projected Gross-Pitaevskii equation, Phys. Rev. A **86**, 053634 (2012).

[49] S. J. Rooney, P. B. Blakie, and A. S. Bradley, Numerical method for the stochastic projected Gross-Pitaevskii equation, Phys. Rev. E **89**, 013302 (2014).

[50] E. Zaremba, T. Nikuni, and A. Griffin, Dynamics of trapped Bose gases at finite temperatures, J. Low Temp. Phys. **116**, 277 (1999).

[51] A. J. Allen, C. F. Barenghi, N. P. Proukakis, and E. Zaremba, A dynamical self-consistent finite-temperature kinetic theory: The ZNG scheme, in *Quantum Gases: Finite Temperature and Non-Equilibrium Dynamics*, Cold Atoms, Vol. 1, edited by N. Proukakis, S. Gardiner, M. Davis, and M. Szymańska (Imperial College Press, World Scientific, Singapore, 2013), p. 93–105.

[52] See Supplemental Material at http://link.aps.org/supplemental/10.1103/PhysRevA.102.053310 for movies.

[53] youtu.be/DmYjGtJcRKQ (2020), Axial 30nK, AXIAL30NK.MP4 in the Supplemental Material [52].

[54] youtu.be/q0ItfdDurec (2020), Axial 60nK, AXIAL60NK.MP4 in the Supplemental Material [52].

[55] youtu.be/ApzQK4d8dtg (2020), Axial 90nK, AXIAL90NK.MP4 in the Supplemental Material [52].

[56] youtu.be/LKNRC6A3aRk (2020), Shock waves interacting with vortex-antivortex line pairs, SW.MP4 in the Supplemental Material [52].

[57] youtu.be/UcXwBZ7liJE (2020), Axial tube 3D tilt 90nK, 3D_90NK.MP4 in the Supplemental Material [52].

[58] youtu.be/YO6fEDD-9zI (2020), Axial 90nK TOF twait 26ms, AXIAL90NKTOF.MP4 in the Supplemental Material [52].

[59] P. H. Roberts and J. Grant, Motions in a Bose condensate. I. The structure of the large circular vortex, J. Phys. A: Gen. Phys. **4**, 55 (1971).

[60] C. A. Jones and P. H. Roberts, Motions in a Bose condensate. IV. Axisymmetric solitary waves, J. Phys. A: Math. Gen. **15**, 2599 (1982).

[61] G. C. Katsimiga, S. I. Mistakidis, G. M. Koutentakis, P. G. Kevrekidis, and P. Schmelcher, Many-body dissipative flow of a confined scalar Bose-Einstein condensate driven by a Gaussian impurity, Phys. Rev. A **98**, 013632 (2018).

[62] W. L. Wang, P. G. Kevrekidis, and E. Babaev, Ring dark solitons in three-dimensional Bose-Einstein condensates, Phys. Rev. A **100**, 053621 (2019).

[63] A. Muñoz Mateo and V. Delgado, Effective mean-field equations for cigar-shaped and disk-shaped Bose-Einstein condensates, Phys. Rev. A **77**, 013617 (2008).

[64] A. Mūnoz Mateo and V. Delgado, Effective one-dimensional dynamics of elongated Bose-Einstein condensates, Ann. Phys. (NY) **324**, 709 (2009).

[65] A. M. Mateo and V. Delgado, Accurate one-dimensional effective description of realistic matter-wave gap solitons, J. Phys. A: Math. Theor. **47**, 245202 (2014).

[66] P. Massignan and M. Modugno, One-dimensional model for the dynamics and expansion of elongated Bose-Einstein condensates, Phys. Rev. A **67**, 023614 (2003).

[67] N. K. Lowman and M. A. Hoefer, Fermionic shock waves: Distinguishing dissipative versus dispersive regularizations, Phys. Rev. A **88**, 013605 (2013).